Editors' Suggestion

# Angle-Resolved Thermal Emission Spectroscopy Characterization of Non-Hermitian Metacrystals

Fan Zhong,[1,2,*] Kun Ding,[3,4] Ye Zhang,[2] Shining Zhu,[2] C.T. Chan,[3] and Hui Liu[2,‡]

[1] *School of Physics, Southeast University, Nanjing 211189, China*

[2] *National Laboratory of Solid State Microstructures & School of Physics, Collaborative Innovation Center of Advanced Microstructures, Nanjing University, Nanjing, Jiangsu 210093, China*

[3] *Department of Physics, Hong Kong University of Science and Technology and William Mong Institute of Nano Science and Technology, Clear Water Bay, Kowloon, Hong Kong, China*

[4] *The Blackett Laboratory, Department of Physics, Imperial College London, London SW7 2AZ, United Kingdom*

(Received 9 December 2019; published 31 January 2020)

We establish angle-resolved thermal emission spectroscopy as an alternative platform to characterize the intrinsic eigenmode properties of non-Hermitian systems. This method can directly map the dispersion of metacrystals within the light cone with high angular resolution. To illustrate its usefulness, we demonstrate the existence of bound states in the continuum (BICs) and non-Hermitian Fermi arcs in a planar corrugated metacrystal by measuring its angle-resolved thermal emission spectra. We show that a change in the thickness of the metacrystal can induce a band inversion between a BIC and a radiative state, and a pair of exceptional points emerge when the band inversion occurs. With this approach, the band mapping of non-Hermitian photonic systems can become a relatively straightforward task.

DOI: 10.1103/PhysRevApplied.13.014071

## I. INTRODUCTION

Angle-resolved photoemission spectroscopy (ARPES) has proved to be an important tool for measuring the energy and momentum of electrons in solids and has provided indispensable insights into the physics of many important materials, from superconductors to topological materials [1]. ARPES requires an external light source to excite and eject the electrons. In order to obtain good resolution of energy and momentum, sophisticated and complex light sources are necessary. In physical systems such as cold atoms and optical systems, the band dispersion is typically determined through various optical excitation methods, including photoexcitation emission [2,3], the reflection spectrum [4], and near-field microwave probes [5]. All these measurements also require external excitation, in which the external light source excites eigenmodes inside the material, and the energy and momentum of the scattered photons are recorded to determine the band dispersion. Here, we demonstrate an angle-resolved thermal emission spectroscopy (ARTES) method which can perform band mapping without an external source. This method is simple and fast, and has excellent angle and frequency resolution, so that the measured "width" of the band is intrinsic and contains information about the coupling coefficient of the state with other degrees of freedom, such as the coupling to free-space photons. As such, ARTES provides a natural platform to explore non-Hermitian physics.

The physics of non-Hermitian systems in photonics, as a generalization of parity-time symmetry [6], has attracted much attention recently. The realization is usually done by inducing gain and/or loss in a photonic system [4,7–18], leading to a wealth of potential applications based on exceptional points (EPs) [11,19–27]. Most finite-sized photonic structures are naturally non-Hermitian, as they have radiative losses, but symmetry-protected radiationless states can appear in many optical systems [28–37]. In addition, the recent development of topological concepts introduces extra degrees of freedom into non-Hermitian physics, and an interplay among geometry, symmetry, and topology is frequently associated with the emergence of EPs [38–47]. In particular, an EP can be regarded as a fractional topological charge, and hence the trajectories of eigenmodes joining EPs of opposite chirality are sometimes called Fermi arcs [42]. EPs can also form connected structures, such as exceptional rings [43] and surfaces [44], in photonic structures. This shows that non-Hermiticity can lead to numerous interesting phenomena, and therefore it is highly desirable to investigate them experimentally.

Our ARTES setup can achieve excellent angular resolution in the infrared region while maintaining simplicity

*zhongfan@seu.edu.cn

‡liuhui@nju.edu.cn

 

of measurement. Compared with ARPES, a light source is unnecessary for constructing an ARTES setup, since the eigenmodes of the sample radiate naturally under thermal excitation. To demonstrate the ability of ARTES, a planar metacrystal whose dispersion can be flexibly tuned by changing its structural parameters is designed and fabricated. By utilizing the symmetry of the structure and the radiation loss, non-Hermitian dispersion features such as bound states in the continuum (BICs), bulk Fermi arcs, and exceptional lines (ELs) are investigated through ARTES in a synthetic parameter space. Both the real and the imaginary parts of the eigenfrequencies can be obtained from the measurements.

## II. ANGLE-RESOLVED THERMAL EMISSION SPECTROSCOPY AND STRUCTURE DESIGN

The experimental setup of the ARTES measurement is shown in Fig. 1(a). Here, our sample is placed in a heater (Linkam FTIR600) to keep the temperature at 100°C with a temperature stability within 0.1°C. The sample, embedded within the heater, is placed on a rotational stage, with the minimum step of rotation being 0.2°. We rotate the sample around the $z$ axis and collect the emission from the sample through the heater window. The distance between the sample and the detector is about 1 m, which is large compared with the wavelength, ensuring excellent angular resolution. The thermal emission signal is analyzed using Fourier transform infrared (FTIR) spectroscopy (Bruker Vertex 70) at various angles, where a polarizer is used to ensure that only TE waves ($E_z$) are recorded by the FTIR spectrometer. The working frequency is chosen at around 30 THz in the atmospheric window, and the resolution of frequency is 0.03 THz (1 $cm^{-1}$), which is high enough for the measurement. The band mapping can be realized without an external probe source. The simplicity and stability of ARTES will make it useful for characterizing applicable devices. The high resolution, both in angle and in frequency, also ensures that the measured width of the band is intrinsic and the real and imaginary parts of the dispersion can be meaningfully extracted to provide insight into non-Hermitian physics.

The design of metacrystals with flexible tuning parameters is first discussed. Prototypes of the designed samples are shown in Fig. 1. A side-view SEM image of one unit cell is shown in Fig. 1(b), and a corresponding schematic with structural parameters is given in Fig. 1(c). The thickness of the underlying Ge layer ($h_a$), the size of the Au grating blocks (height $h_d$ and width $d_b$), and the gap width ($d_a$) between two adjacent Au blocks are fixed after photolithography. However, the thickness of the top Ge layer ($h_b$) can be continuously changed by depositing additional Ge on top of the Au grating, and hence $h_b$ can function as a tunable parameter. Figure 1(d) shows a top view of a small portion of the whole sample. The thermal emission of this metacrystal is measured with ARTES. In this experiment, the ARTES measurement is carried out and the value of $h_b$ is changed alternately, thereby obtaining thermal emission spectra with various values of $h_b$.

In the experiment, the structure is fabricated on a silicon wafer (2 × 1.6 $cm^2$) according to the design in Fig. 1(c). A 200 nm gold layer and a Ge layer with thickness $h_a$ are first deposited by electron-beam evaporation (EBE). Afterwards, the gold grating is fabricated by photolithography with a width $d_b$, thickness $h_d$, and period $\Lambda = d_a + d_b$. A Ge layer is again deposited on the grating, with the designed thickness $h_b$, by EBE.

## III. NUMERICAL SIMULATIONS FOR BICS AND EPS

We focus on the guided mode in the Ge layer of the designed structure shown in Fig. 1(b). Both the real and the imaginary part (Re($n$) and Im($n$)) of the

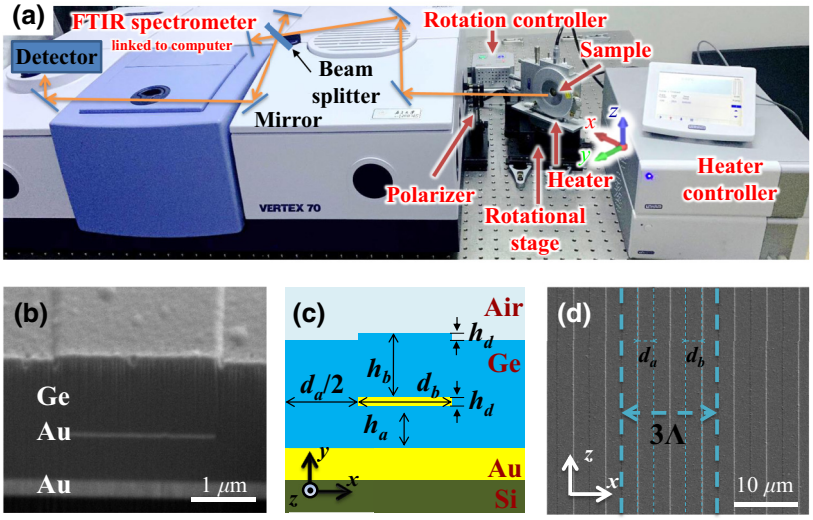


FIG. 1. ARTES setup and structure of the metacrystal. (a) Picture and schematic of the ARTES setup. The sample is heated inside the heater, with a window to output the signals. The heater is placed on a precisely controlled electric rotational stage. (b) SEM side view of one sample. The dark region is germanium (Ge), and the gray strip in the middle is a gold grating. (c) Schematic of the unit cell, with structural parameters $h_a$, $h_b$, $h_d$, and $\Lambda = d_a + d_b$. (d) SEM top view of a sample with structure parameters $d_a$, $d_b$, and $\Lambda$, marked by the cyan dashed lines.

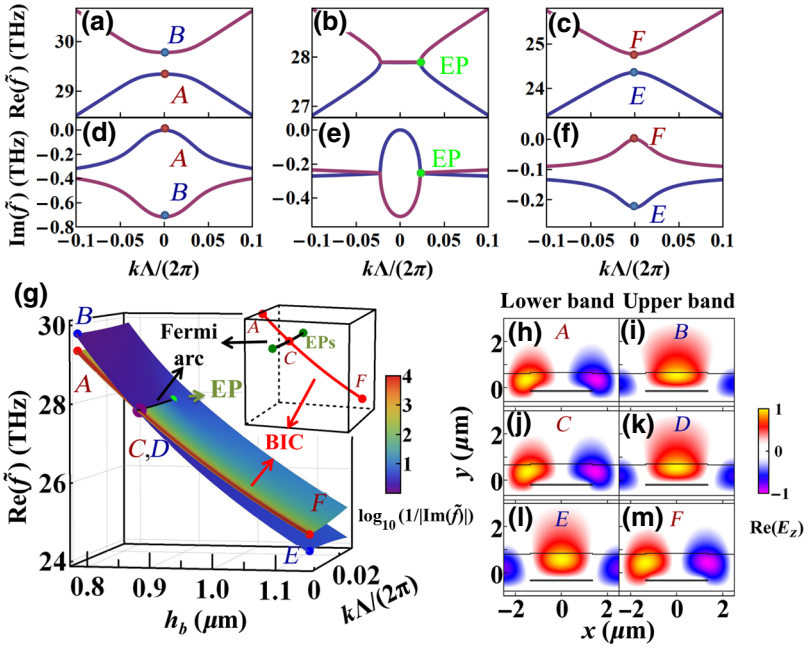


FIG. 2. Calculated band structures and eigenmode profiles. Calculated dispersion of real [(a)–(c) ] and imaginary [(d)–(f)] frequencies for different $h_b$ parameters: (a), (d) $h_b = 0.78\,\mu$m; (b), (e) $h_b = 0.877\,\mu$m; (c), (f) $h_b = 1.15\,\mu$m. Au is described by a lossless Drude model with $\varepsilon_{\mathrm{Au}} = 1 - \omega_p^2/\omega^2$ ($\omega_p = 9.0$ eV) and $\varepsilon_{\mathrm{Ge}} = 16.04$. The structural parameters are $\Lambda = 5\,\mu$m, $d_a = 2.7\,\mu$m, $d_b = 2.3\,\mu$m, $h_a = 0.44\,\mu$m, and $h_d = 45$ nm. The three cases in (a)–(f) correspond to the three sections shown in (g). (g) Dispersion of real part of eigenfrequencies $\mathrm{Re}(\tilde{f})$ of TE modes in the synthetic parameter space $(k, h_b)$, calculated with COMSOL. The color of the surface represents the inverse of the imaginary parts of the eigenfrequencies $\mathrm{Im}(\tilde{f})$ on a $\log_{10}$ scale. The black line denotes the modes with identical real parts of the eigenfrequencies (also referred as a bulk Fermi arc in the case of a non-Hermitian system) linking two EPs (green dots). The inset shows the crossing between the BIC (red line) and the bulk Fermi arc (black line). (h)–(m) $E_z$ field profile of eigenmodes, with their parameters $[\mathrm{Re}(\tilde{f}),\ k\Lambda/(2\pi), h_b]$ given as (A) (29.349 THz, 0, 0.78 $\mu$m), (B) (29.785 THz, 0, 0.78 $\mu$m), (C) (27.852 THz, 0, 0.8797 $\mu$m), (D) (27.852 THz, 0, 0.8797 $\mu$m), (E) (24.357 THz, 0, 1.15 $\mu$m), and (F) (24.774 THz, 0, 1.15 $\mu$m).

effective mode index of the multilayer structure can be controlled by the geometric parameters of the Au cladding grating and the Ge layer. The Au blocks significantly enhance the contrast of $\mathrm{Re}(n)$, and the tunable parameter $h_b$ can control the difference in $\mathrm{Im}(n)$ between two guided modes in the Ge layer. To guide the design of BICs and EPs, an effective one-dimensional metacrystal model is established to describe the system, in which each multilayer region is treated as an effective homogeneous layer with an effective mode index [48] (see Sec. I of the Supplemental Material [49]). This model shows that the tuning parameters can induce a band inversion of BICs with a radiative state, leading to a pair of EPs connected by a non-Hermitian Fermi arc.

To reassure ourselves that the model provides a correct prediction before performing the experiment, the dispersion of TE-polarized guided modes of the metacrystal is investigated for different values of $h_b$ using full-wave simulations with COMSOL [50]. The calculated dispersions of $\mathrm{Re}(\tilde{f})$ for three values of $h_b$ are given in Figs. 2(a)–2(c), and the corresponding dispersions of $\mathrm{Im}(\tilde{f})$ are given in Figs. 2(d)–2(f). A gap between two photonic bands is seen at $h_b = 0.78\,\mu$m. The gap becomes smaller as $h_b$ increases. The gap closes at $h_b = 0.877\,\mu$m, and a pair of EPs appear. A further increase of $h_b$ opens up the gap again, as shown in Fig. 2(c). In order to give a holistic view of the evolution of the dispersions, we plot in Fig. 2(g) the real parts of the eigenfrequencies $\mathrm{Re}(\tilde{f})$ in a two-dimensional (2D) synthetic parameter space $(k, h_b)$. The color of the surface represents the inverse of the imaginary parts of the eigenfrequencies $\mathrm{Im}(\tilde{f})$. A BIC line at $k = 0$ can be clearly seen, which is mandated by symmetry. At $h_b = 0.78\,\mu$m, mode B, at the upper band edge ($k = 0$), has a much larger $\mathrm{Im}(\tilde{f})$ than that of mode A. This indicates that mode B has a larger radiation damping, and its mode profile is plotted in Fig. 2(i). In contrast, $\mathrm{Im}(\tilde{f})$ of mode A at $k = 0$ is almost zero ($< 10^{-7}$ THz), and its mode profile is shown in Fig. 2(h). It can be seen that mode A is antisymmetric about $x = 0$, but mode B is symmetric about $x = 0$. This illustrates that the mode profile of mode A does not match that of light in free space and, as such, is a BIC. Figures 2(a) and 2(d) show that all the nearby modes except A are radiative ones. Such a symmetry always holds when

$h_b$ is varied. Therefore, modes A, C, and F are all BICs at $k=0$, similar to the BICs that have appeared in other optical systems [33], which can be utilized to manipulate thermal emission [51,52].

With an increase in $h_b$, the contrast in both Re($n$) and Im($n$) between these two multilayer regions decreases monotonically. This provides two competitive mechanisms for changing the band gap. A decrease in the contrast of Re($n$) will reduce the gap, while a decrease in the difference in Im($n$) will enlarge the gap. Therefore, the two bands will "meet" at a certain $h_b$, which is confirmed in Fig. 2(g). We find that at $h_b = 0.877\,\mu$m, a pair of EPs appears at $k\Lambda/(2\pi) = \pm 0.0227$ and $\tilde{f} = (27.891 - 0.24857i)$ THz, which are marked by green dots. Note that at $k=0$, the bound mode C and the radiative mode D are orthogonal by symmetry, which can be seen from their mode profiles in Figs. 2(j) and 2(k). They cannot couple, and the coupling coefficient must be zero at $k=0$. However, the coupling coefficient is nonzero at finite $k$, and an EP can appear at a particular $k$ value if the coupling coefficient is equal to the difference in radiation damping. The EPs must come in plus and minus $k$ pairs due to parity symmetry, and the gap-closing points between such pairs of EPs are connected to form a bulk Fermi arc in a non-Hermitian system, as shown by the black line in Fig. 2(g). This is because the line links two EPs with topological charges $\pm 1/2$ [42] (see Sec. II of the Supplemental Material [49]). The bulk Fermi arc intersects the BIC modes denoted by the solid red curve $\widehat{ACF}$ at C, as shown in the inset of Fig. 2(g). It is also worthy of mention that for smaller $h_b$, the less radiative band carrying the BIC at $k=0$ has a lower Re($\tilde{f}$) in frequency, while for larger $h_b$, the less radiative band has a higher Re($\tilde{f}$) in frequency. The change in $h_b$ induces a topological band inversion, since the symmetric and antisymmetric modes swap their positions [53] (see Sec. III of the Supplemental Material [49]).

## IV. RESULTS

### A. Experimental observation of BICs and EPs

The dispersion of the metacrystals is measured with ARTES. The experimental and corresponding simulation results are compared in Fig. 3. It is not easy to directly calculate the far-field thermal radiation, and hence the absorption spectra instead are calculated according to Kirchhoff's law [54]. Figures 3(a)–3(c) show the optical absorption spectra calculated using the simulation software Lumerical FDTD, at different incident angles for three values of $h_b$ (see Sec. IV of the Supplemental Material for details [49]). To quantitatively compare the calculations with the measured results, the permittivities of gold and germanium retrieved from the experimental data using finite-difference time-domain (FDTD) simulations are used [55]. The measured thermal emission spectra are shown in Figs. 3(d)–3(f), and agree well with the FDTD results. Two bands can be clearly seen in the spectra, and their intensities vary dramatically with $h_b$. For $h_b = 0.816$ and $1.15\,\mu$m in Figs. 3(a), 3(c), 3(d), and 3(f), the modes marked with red dots at $k=0$ show very small amounts of radiation (or absorption). These modes correspond to the BICs displayed in Fig. 2. Around $h_b = 0.8784\,\mu$m, a band inversion occurs, and the BIC transits from the lower to the upper band, indicating a topological transition when the band gap closes. The spectra in Figs. 3(b) and 3(e) indicate that a pair of EPs appears at $k\Lambda/(2\pi) = \pm 0.0220$, near the transition point. For comparison, the real parts of the eigenfrequencies Re($\tilde{f}$) calculated by COMSOL are plotted as blue dashed lines in Figs. 3(a)–3(f). The good agreement between the measurements and calculations corroborates the existence of a pair of EPs at a specific value of $h_b$.

Besides the real parts of the eigenfrequencies Re($\tilde{f}$), the imaginary parts Im($\tilde{f}$) are required to determine both the BICs and the EPs. As the quality factors of the emission curves are related to Im($\tilde{f}$) [shown in Figs. 2(d)–2(f)], Im($\tilde{f}$) can be retrieved from the experimental spectra. Figures 3(g)–3(i) show the emission spectra for three samples at wave vectors $k\Lambda/(2\pi) = 0$ (purple dots) and $k\Lambda/(2\pi) = 0.06$ (red dots), which are correspondingly labeled by magenta and red dashed lines in Figs. 3(d)–3(f). For $k\Lambda/(2\pi) = 0.06$, there are two emission peaks, originating from two photonic bands. However, for $k\Lambda/(2\pi) = 0$, only one emission peak appears, due to the disappearance of the BIC emission peaks. To retrieve Im($\tilde{f}$), Lorentzian line-shape functions are used to fit the emission spectra in Figs. 3(g)–3(i). The eigenfrequencies are retrieved through fitting the measured thermal emission spectra using the function

$$I = I_0 + \left( \sum_j \frac{t_j}{f - \left[ \mathrm{Re}\left(\tilde{f}_j\right) + i\,\mathrm{Im}\left(\tilde{f}_j\right) \right]} \right) \times \left( \sum_j \frac{t_j}{f - \left[ \mathrm{Re}\left(\tilde{f}_j\right) + i\,\mathrm{Im}\left(\tilde{f}_j\right) \right]} \right)^* .$$

Here, $I$ is the intensity, $I_0$ is the background intensity, $t_j$ are the complex fitting parameters, and $f$ is the experimental frequency. In Figs. 3(g)–3(i), the solid lines are fitted curves of Lorentzian line-shape functions, which fit the experiment spectra quite well. The retrieved values of Im($\tilde{f}$) are plotted as blue squares in Figs. 3(j)–3(l), which are compared with COMSOL calculations shown by blue dashed lines. The Im($\tilde{f}$) values extracted from the measurements agree with the COMSOL calculations. Especially, the extracted Im($\tilde{f}$) in Fig. 3(k) confirms the EP at $h_b = 0.8755\,\mu$m depicted in Figs. 3(b) and 3(e). If the values of Im($\tilde{f}$) for the three samples in Figs. 3(j)–3(l) are

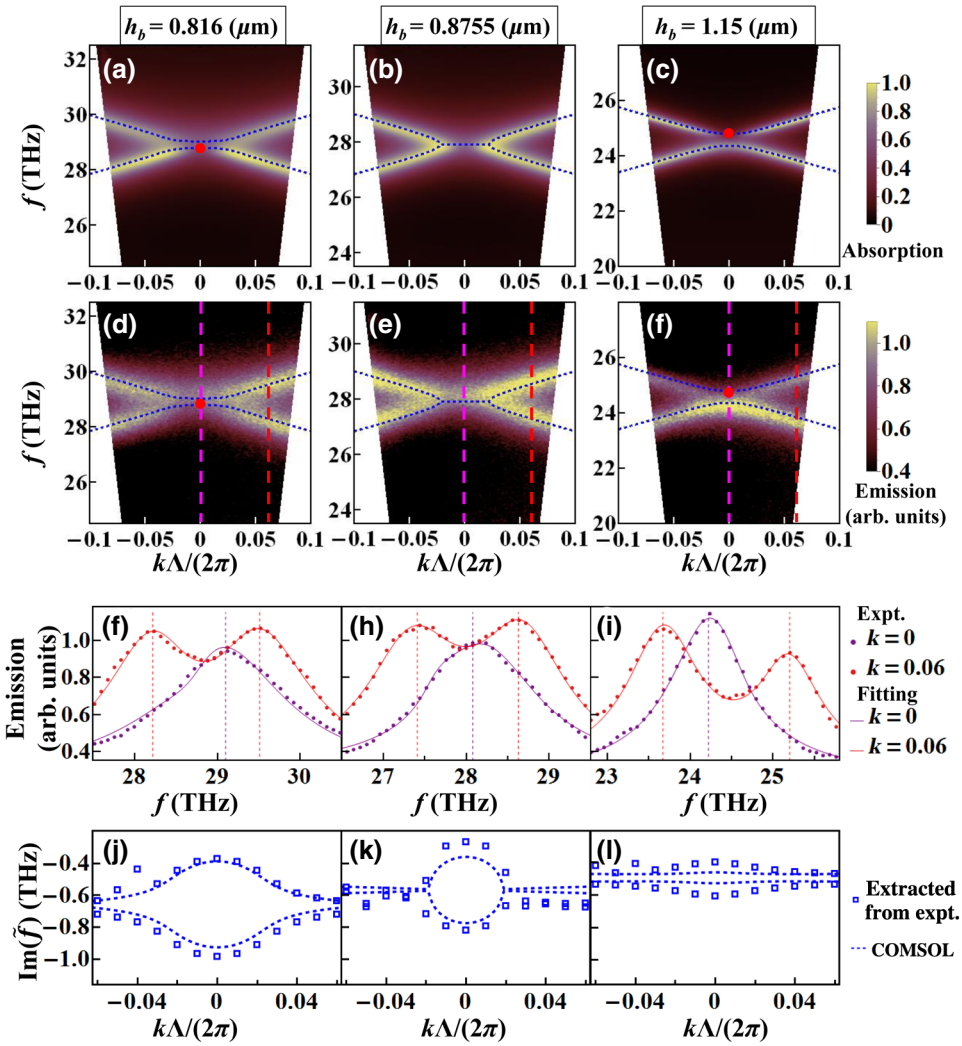


FIG. 3. Experimental observation and numerical simulations of EPs and BICs. (a)–(c) Optical absorption simulated by FDTD simulations with realistic material parameters ("Au-Palik" and "Ge-Palik" from the FDTD material database [55]) and (d)–(f) measured thermal emission: (a), (d) $h_b = 0.816\,\mu$m; (b), (e) $h_b = 0.8755\,\mu$m; (c), (f) $h_b = 1.15\,\mu$m. The blue dashed lines in (a)–(f) are eigenfrequencies calculated by COMSOL with the Drude model [$\varepsilon_{\mathrm{Au}} = 1 - \omega_p^2/(\omega^2 + i\omega\omega_c)$, $\omega_p = 9.0$ eV, and $\omega_c = 0.027$ eV]. Here, the structure parameters are $\Lambda = 5\,\mu$m, $d_a = 2.7\,\mu$m, $d_b = 2.3\,\mu$m, $h_a = 0.44\,\mu$m, and $h_d = 45$ nm. The measurement resolution in (d)–(f) is $\delta k \sim \delta\theta/\lambda \approx 0.02^\circ/\mu$m. (g)–(i) The solid dots are thermal emission spectra, with wave vectors marked by the vertical dashed lines in (d)–(f) at $k\Lambda/(2\pi) = 0$ (purple dots) and $k\Lambda/(2\pi) = 0.06$ (red dots), and the corresponding solid lines are the curves fitted to the dots. In (g)–(i), all the purple lines have one resonance peak, and the red curves have two resonance peaks. The resonance frequency of the peak in the purple lines is redshifted with increasing $h_b$. In (j)–(l), blue square dots show the imaginary part of the eigenfrequencies extracted from experimental data shown in (d)–(f). The blue dashed lines are calculated by COMSOL with the Drude model [$\omega_p = 9.0$ eV, $\omega_c = 0.162$ eV in (j) and (k), and $\omega_c = 0.324$ eV in (l)].

compared, the absolute values of $\mathrm{Im}(\tilde{f})$ decrease with an increase in $h_b$. This is because, for larger $h_b$, guided modes can be better confined inside the metacrystal and the radiation loss is reduced, leading to smaller absolute values of $\mathrm{Im}(\tilde{f})$.

### B. BIC lines and Fermi arcs in synthetic dimensions

In order to compare the above experiments with the theoretical calculations shown in Fig. 2(g), Fig. 4(a) shows the measured real parts of the eigenfrequencies $\mathrm{Re}(\tilde{f})$ in the 2D synthetic parameter space ($k$, $h_b$). The color of each dot represents the inverse of the experimentally extracted $|\mathrm{Im}(\tilde{f})|$. The results for eight samples with different values of $h_b$ are shown in Fig. 4(a); details of the experiments and simulations are given in Fig. S5 in the Supplemental Material [49]. Most dots are in blue, but there exists a string of red dots at $k\Lambda/(2\pi) = 0$, corresponding to BICs mandated by symmetry. However, the color contrast between BICs and other radiative modes in Fig. 4(a) is smaller than

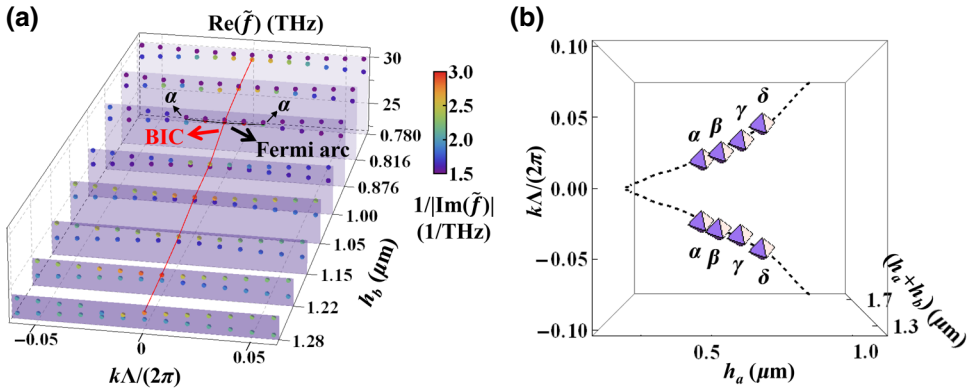


FIG. 4. BIC, Fermi arc, and exceptional lines in synthetic space. (a) Real parts of eigenfrequencies in 2D parameter space ($k$, $h_b$), which are read from the experimental data in Fig. 3. The data are plotted as filled dots with their colors denoting different imaginary parts of the eigenfrequencies. The BIC line and bulk Fermi arc calculated by COMSOL are shown as red and black curves, respectively. (b) Exceptional lines in 3D parameter space ($k$, $h_a$, $h_a + h_b$). Here, the parameters are set to $d_b = 2.3\ \mu$m, $\Lambda = 5\ \mu$m, $h_d/h_a = 45/440$, while $h_a$ and $h_b$ are variables. The measured EP pairs are represented as dots marked $\alpha$, $\beta$, $\gamma$, $\delta$. In the experiment, four samples are fabricated, with their parameters ($h_a$, $h_a + h_b$) given as $\alpha$ (0.44 $\mu$m, 1.3155 $\mu$m), $\beta$ (0.51 $\mu$m, 1.3732 $\mu$m), $\gamma$ (0.6 $\mu$m, 1.4575 $\mu$m), and $\delta$ (0.7 $\mu$m, 1.5242 $\mu$m).

that in Fig. 2(g), because ohmic losses in the gold grating [which are not included in Fig. 2(g)] contribute to Im($\tilde{f}$) and reduce the quality factors of the BICs in the experiment. Nevertheless, in Fig. 4(a), the |Im($\tilde{f}$)| values of the BICs are still local minima of emission. Varying $h_b$ induces a band inversion of two bands at $h_b \cong 0.878\ \mu$m. At this transition point, a bulk Fermi arc connects two EPs, shown as a solid black line in the 2D synthetic parameter space in Fig. 4(a). The BIC line intersects with the bulk Fermi arc at $k\Lambda/(2\pi) = 0$ and $h_b \cong 0.878\ \mu$m in the synthetic parameter space.

### C. Exceptional lines in synthetic dimensions

In the above discussion, a pair of EPs is shown at one particular value of $h_b$. Actually, more EPs can be found in a higher-dimensional space. In Fig. 1(b), besides $h_b$, the thickness $h_a$ can also be used as another synthetic parameter. In a new design, $h_a$ and $h_b$ are chosen as independent tunable parameters, and the other parameters ($d_b$, $\Lambda$, and $h_d$) are fixed. A three-dimensional (3D) synthetic parameter space is constructed using ($k$, $h_a$, $h_a + h_b$). When these parameters are scanned in COMSOL simulations, all the EPs obtained in this 3D synthetic space form ELs, which are shown as black dashed lines in Fig. 4(b). As the EPs always appear in pairs at two wave vectors $k$ and $(-k)$ in reciprocal systems, there are two ELs which are symmetric with respect to the $k = 0$ plane. The two dashed lines are degenerate at $k\Lambda/(2\pi) = 0$, indicating a pair of EPs originating from the degeneracy at the $\Gamma$ point. In the experiment, four samples are fabricated, and their EPs can be determined by ARTES [represented as dots in Fig. 4(b)]. The results for sample $\alpha$ are already provided in Fig. 3, and the results for the other three samples ($\beta$, $\gamma$, $\delta$) are provided in Fig. S6 in the Supplemental Material [49]. All the measured EPs are well located on the calculated dashed line, implying good agreement between the calculations and measurements.

## V. CONCLUSIONS

We design and experimentally realize metallic metacrystals that can work as a flexible system to investigate various non-Hermitian and topological physics. These metacrystals exhibit symmetry-protected BICs. Through changing the thickness of the cover layer above the metacrystal, the radiative losses of the metacrystal can be controlled to induce band inversions. At the crossover point, EPs and an associated non-Hermitian Fermi arc can be observed linking them. Various features in synthetic parameter spaces, such as the trajectories of BICs and bulk Fermi arcs, can be mapped using the ARTES platform with high angular resolution. The interesting physics studied here can be utilized to manipulate thermal emission, including emission spectra and radiation patterns. For example, a BIC can suppress the thermal emission in one particular direction, which can be useful in thermophotovoltaic devices and radiative cooling. In addition, as optical absorption is the reverse process of thermal emission (from the point of view of Kirchhoff's law), this scheme can also be used to control optical absorption of light coming from the far field.

More importantly, this paper demonstrates the usefulness of a home-made ARTES platform which offers a simple but powerful experimental technique to characterize the dispersion of non-Hermitian systems. It has

excellent angular resolution and operates in a broad frequency range, from the near to the far infrared. It will be a useful tool for exploring the topological band structures of non-Hermitian photonic-crystal slabs consisting of various microstructures types.

## ACKNOWLEDGMENTS

This work was financially supported by the National Natural Science Foundation of China (Grants No. 11690033, No. 61425018, and No.11621091) and the National Key Research and Development Program of China (Grants No. 2017YFA0205700 and No. 2017YFA0303702). Work done in Hong Kong was supported by the Research Grants Council (RGC) Hong Kong through Grants No. N_HKUST608/17 and No. AoE/P-02/12. K.D. acknowledges funding from the Gordon and Betty Moore Foundation.

F.Z., K.D. and Y.Z. contributed equally to this work.

[1] A. Damascelli, Z. Hussain, and Z.-X. Shen, Angle-resolved photoemission studies of the cuprate superconductors, Rev. Mod. Phys. **75**, 473 (2003).

[2] T. L. Dao, A. Georges, J. Dalibard, C. Salomon, and I. Carusotto, Measuring the One-Particle Excitations of Ultracold Fermionic Atoms by Stimulated Raman Spectroscopy, Phys. Rev. Lett. **98**, 240402 (2007).

[3] J. T. Stewart, J. P. Gaebler, and D. S. Jin, Using photoemission spectroscopy to probe a strongly interacting Fermi gas, Nature **454**, 744 (2008).

[4] B. Zhen, C. W. Hsu, Y. Igarashi, L. Lu, I. Kaminer, A. Pick, S. L. Chua, J. D. Joannopoulos, and M. Soljacic, Spawning rings of exceptional points out of Dirac cones, Nature **525**, 354 (2015).

[5] B. Yang, *et al.*, Ideal Weyl points and helicoid surface states in artificial photonic crystal structures, Science **359**, 1013 (2018).

[6] C. M. Bender and S. Boettcher, Real Spectra in Non-Hermitian Hamiltonians Having PT Symmetry, Phys. Rev. Lett. **80**, 5243 (1998).

[7] A. Guo, G. J. Salamo, D. Duchesne, R. Morandotti, M. Volatier-Ravat, V. Aimez, G. A. Siviloglou, and D. N. Christodoulides, Observation of PT-Symmetry Breaking in Complex Optical Potentials, Phys. Rev. Lett. **103**, 093902 (2009).

[8] C. E. Rüter, K. G. Makris, R. El-Ganainy, D. N. Christodoulides, M. Segev, and D. Kip, Observation of parity–time symmetry in optics, Nat. Phys. **6**, 192 (2010).

[9] A. Regensburger, C. Bersch, M. A. Miri, G. Onishchukov, D. N. Christodoulides, and U. Peschel, Parity-time synthetic photonic lattices, Nature **488**, 167 (2012).

[10] B. Peng, *et al.*, Parity–time-symmetric whispering-gallery microcavities, Nat. Phys. **10**, 394 (2014).

[11] L. Chang, X. Jiang, S. Hua, C. Yang, J. Wen, L. Jiang, G. Li, G. Wang, and M. Xiao, Parity–time symmetry and variable optical isolation in active–passive-coupled microresonators, Nat. Photon. **8**, 524 (2014).

[12] Y. D. Chong, L. Ge, and A. D. Stone, PT-Symmetry Breaking and Laser-Absorber Modes in Optical Scattering Systems, Phys. Rev. Lett. **106**, 093902 (2011).

[13] S. Zhang, Z. Ye, Y. Wang, Y. Park, G. Bartal, M. Mrejen, X. Yin, and X. Zhang, Anti-Hermitian Plasmon Coupling of an Array of Gold Thin-Film Antennas for Controlling Light at the Nanoscale, Phys. Rev. Lett. **109**, 193902 (2012).

[14] Y. Sun, W. Tan, H. Q. Li, J. Li, and H. Chen, Experimental Demonstration of a Coherent Perfect Absorber with PT Phase Transition, Phys. Rev. Lett. **112**, 143903 (2014).

[15] A. Cerjan, A. Raman, and S. Fan, Exceptional Contours and Band Structure Design in Parity-Time Symmetric Photonic Crystals, Phys. Rev. Lett. **116**, 203902 (2016).

[16] Z. Lin, A. Pick, M. Loncar, and A. W. Rodriguez, Enhanced Spontaneous Emission at Third-Order Dirac Exceptional Points in Inverse-Designed Photonic Crystals, Phys. Rev. Lett. **117**, 107402 (2016).

[17] L. Feng, R. El-Ganainy, and L. Ge, Non-Hermitian photonics based on parity–time symmetry, Nat. Photon. **11**, 752 (2017).

[18] R. El-Ganainy, K. G. Makris, M. Khajavikhan, Z. H. Musslimani, S. Rotter, and D. N. Christodoulides, Non-Hermitian physics and PT symmetry, Nat. Phys. **14**, 11 (2018).

[19] H. Hodaei, M. A. Miri, M. Heinrich, D. N. Christodoulides, and M. Khajavikhan, Parity-time-symmetric microring lasers, Science **346**, 975 (2014).

[20] L. Feng, Z. J. Wong, R. M. Ma, Y. Wang, and X. Zhang, Single-mode laser by parity-time symmetry breaking, Science **346**, 972 (2014).

[21] B. Peng, S. K. Ozdemir, S. Rotter, H. Yilmaz, M. Liertzer, F. Monifi, C. M. Bender, F. Nori, and L. Yang, Loss-induced suppression and revival of lasing, Science **346**, 328 (2014).

[22] R. Fleury, D. Sounas, and A. Alu, An invisible acoustic sensor based on parity-time symmetry, Nat. Commun. **6**, 5905 (2015).

[23] H. Hodaei, A. U. Hassan, S. Wittek, H. Garcia-Gracia, R. El-Ganainy, D. N. Christodoulides, and M. Khajavikhan, Enhanced sensitivity at higher-order exceptional points, Nature **548**, 187 (2017).

[24] W. Chen, S. Kaya Ozdemir, G. Zhao, J. Wiersig, and L. Yang, Exceptional points enhance sensing in an optical microcavity, Nature **548**, 192 (2017).

[25] S. A. Hassani Gangaraj and F. Monticone, Topological Waveguiding near an Exceptional Point: Defect-Immune, Slow-Light, and Loss-Immune Propagation, Phys. Rev. Lett. **121**, 093901 (2018).

[26] S. Assawaworrarit, X. Yu, and S. Fan, Robust wireless power transfer using a nonlinear parity-time-symmetric circuit, Nature **546**, 387 (2017).

[27] H. Zhao, Z. Chen, R. Zhao, and L. Feng, Exceptional point engineered glass slide for microscopic thermal mapping, Nat. Commun. **9**, 1764 (2018).

[28] Y. Plotnik, O. Peleg, F. Dreisow, M. Heinrich, S. Nolte, A. Szameit, and M. Segev, Experimental Observation of Optical Bound States in the Continuum, Phys. Rev. Lett. **107**, 183901 (2011).

[29] S. Mukherjee, A. Spracklen, D. Choudhury, N. Goldman, P. Ohberg, E. Andersson, and R. R. Thomson, Observation of a Localized Flat-Band State in a Photonic Lieb Lattice, Phys. Rev. Lett. **114**, 245504 (2015).

[30] R. A. Vicencio, C. Cantillano, L. Morales-Inostroza, B. Real, C. Mejia-Cortes, S. Weimann, A. Szameit, and M. I. Molina, Observation of Localized States in Lieb Photonic Lattices, Phys. Rev. Lett. **114**, 245503 (2015).

[31] C. W. Hsu, B. Zhen, J. Lee, S. L. Chua, S. G. Johnson, J. D. Joannopoulos, and M. Soljacic, Observation of trapped light within the radiation continuum, Nature **499**, 188 (2013).

[32] Y. Zhang, *et al.*, Observation of Polarization Vortices in Momentum Space, Phys. Rev. Lett. **120**, 186103 (2018).

[33] A. Cerjan, C. W. Hsu, and M. C. Rechtsman, Bound States in the Continuum through Environmental Design, Phys. Rev. Lett. **123**, 023902 (2019).

[34] Y. X. Xiao, G. Ma, Z. Q. Zhang, and C. T. Chan, Topological Subspace-Induced Bound State in the Continuum, Phys. Rev. Lett. **118**, 166803 (2017).

[35] J. Gomis-Bresco, D. Artigas, and L. Torner, Anisotropy-induced photonic bound states in the continuum, Nat. Photon. **11**, 232 (2017).

[36] S. I. Azzam, V. M. Shalaev, A. Boltasseva, and A. V. Kildishev, Formation of Bound States in the Continuum in Hybrid Plasmonic-Photonic Systems, Phys. Rev. Lett. **121**, 253901 (2018).

[37] X. Gao, B. Zhen, M. Soljačić, H. Chen, and C. W. Hsu, Bound States in the Continuum in Fiber Bragg Gratings, ACS Photonics **6**, 2996 (2019).

[38] H. Shen, B. Zhen, and L. Fu, Topological Band Theory for Non-Hermitian Hamiltonians, Phys. Rev. Lett. **120**, 146402 (2018).

[39] S. Yao, F. Song, and Z. Wang, Non-Hermitian Chern Bands, Phys. Rev. Lett. **121**, 136802 (2018).

[40] Z. Gong, Y. Ashida, K. Kawabata, K. Takasan, S. Higashikawa, and M. Ueda, Topological Phases of Non-Hermitian Systems, Phys. Rev. X **8**, 031079 (2018).

[41] S. Weimann, M. Kremer, Y. Plotnik, Y. Lumer, S. Nolte, K. G. Makris, M. Segev, M. C. Rechtsman, and A. Szameit, Topologically protected bound states in photonic parity-time-symmetric crystals, Nat. Mater. **16**, 433 (2017).

[42] H. Zhou, C. Peng, Y. Yoon, C. W. Hsu, K. A. Nelson, L. Fu, J. D. Joannopoulos, M. Soljacic, and B. Zhen, Observation of bulk Fermi arc and polarization half charge from paired exceptional points, Science **359**, 1009 (2018).

[43] A. Cerjan, S. Huang, M. Wang, K. P. Chen, Y. Chong, and M. C. Rechtsman, Experimental realization of a Weyl exceptional ring, Nat. Photon. **13**, 623 (2019).

[44] H. Zhou, J. Y. Lee, S. Liu, and B. Zhen, Exceptional surfaces in PT-symmetric non-Hermitian photonic systems, Optica **6**, 190 (2019).

[45] H. Zhao, X. Qiao, T. Wu, B. Midya, S. Longhi, and L. Feng, Non-Hermitian topological light steering, Science **365**, 1163 (2019).

[46] Y. Xu, S. T. Wang, and L. M. Duan, Weyl Exceptional Rings in a Three-Dimensional Dissipative Cold Atomic Gas, Phys. Rev. Lett. **118**, 045701 (2017).

[47] K. Ding, G. Ma, M. Xiao, Z. Q. Zhang, and C. T. Chan, Emergence, Coalescence, and Topological Properties of Multiple Exceptional Points and Their Experimental Realization, Phys. Rev. X **6**, 021007 (2016).

[48] M. Born and E. Wolf, *Principles of Optics* (Pergamon, Oxford, 1986), 6th ed.

[49] See the Supplemental Material at http://link.aps.org/supplemental/10.1103/PhysRevApplied.13.014071 for details of the models, simulations, and experiments.

[50] Computer code COMSOL MULTI-PHYSICS 5.3 (developed by COMSOL Inc., Burlington, VT, 2017).

[51] A. P. Raman, M. A. Anoma, L. Zhu, E. Rephaeli, and S. Fan, Passive radiative cooling below ambient air temperature under direct sunlight, Nature **515**, 540 (2014).

[52] O. Ilic, P. Bermel, G. Chen, J. D. Joannopoulos, I. Celanovic, and M. Soljacic, Tailoring high-temperature radiation and the resurrection of the incandescent source, Nat. Nanotechnol. **11**, 320 (2016).

[53] M. Xiao, Z. Q. Zhang, and C. T. Chan, Surface Impedance and Bulk Band Geometric Phases in One-Dimensional Systems, Phys. Rev. X **4**, 021017 (2014).

[54] X. Liu, T. Tyler, T. Starr, A. F. Starr, N. M. Jokerst, and W. J. Padilla, Taming the Blackbody with Infrared Metamaterials as Selective Thermal Emitters, Phys. Rev. Lett. **107**, 045901 (2011).

[55] Lumerical Solutions, Inc. http://www.lumerical.com/tcad-products/fdtd/